XL CILAMCE
IBERO-LATIN AMERICAN CONGRESS ON COMPUTATIONAL METHODS IN ENGINEERING
NOVEMBER 11-14, 2019
Praiamar Natal Hotel & Convention
Natal, RN-BRAZIL

PREDICTION OF INSERTION LOSS OF THIN ACOUSTIC BARRIERS USING THE METHOD OF FUNDAMENTAL SOLUTIONS

Edmundo G. de A. Costa
edmundo_costa@coc.ufrj.br
Department of Civil Engineering, COPPE – Federal University of Rio de Janeiro
Ilha do Fundão, CP 68506, CEP 21945-970, Rio de Janeiro, RJ, Brazil
Samuel B. Velten
samuelbv2004@yahoo.com.br
Department of Mechanics Engineering, IFES – Federal Institute of Espírito Santo
Morobá, CEP 29192-733, Aracruz, Espírito Santo, ES, Brazil
Wilian J. dos Santos
wilianj@ufrrj.br
Department of Mathematics, Rural Federal University of Rio de Janeiro
Seropédica, CEP 23897-000, Rio de Janeiro, RJ, Brazil
José A. F. Santiago
santiago@coc.ufrj.br
Department of Civil Engineering, COPPE – Federal University of Rio de Janeiro
Ilha do Fundão, CP 68506, CEP 21945-970, Rio de Janeiro, RJ, Brazil

Abstract. In this paper, the Method of Fundamental Solutions (MFS) is applied to predict the insertion loss of thin acoustic barriers on a rigid ground in the vicinity of a tall building. The MFS formulation makes use of suitable Green's functions defined by the image-source technique, allowing decreasing the number of discretized surfaces and consequently reducing the computational cost of the numerical model. Both the ground and the building are modeled as infinite rigid plane surfaces. To validate the implementation of the proposed formulation, the MFS results are compared with those provided by the Dual-BEM formulation. Numerical simulations are carried out in order to illustrate the acoustic performance of thin barriers of different shapes for typical cases of traffic noise.

Keywords: Method of Fundamental Solutions, Dual-BEM formulation, Green's functions, Image-source technique

1 Introduction

Acoustic barriers are widely used to reduce the noise pollution and to shield residencial areas from the traffic noise. Different types of barriers are used to obstruct the sightline between the observer and the sound source. Many numerical methods have been developed to simulate sound propagation around the acoustic barriers. Among them, the Boundary Element Method (BEM) has a more compact description of the acoustic medium, requiring only the discretization of the boundaries of the problem and it is very well suited to simulate of homogeneous unbounded problems since it automatically satisfies the Sommerfeld radiation condition. The BEM has a number of advantages over other methods [1]. However, its application is often limited by the requirement of prior knowledge of Green's functions and the appearance of numerical and analytical integrals, and has some difficulties for analysis of very thin bodies, in the form of near-singularities and near-degeneracy of the final system of equations.

Filippi and Dumery [2], Cassot [3] and Terai [4] developed an efficient boundary integral equation technique to analyse the scattering of waves by thin rigid screens in infinite domain. Later, Kawai and Terai [5] applied the standard and hyper-singular integral equations to analyse outdoor sound attenuation by thin absorbing barriers over a rigid ground using a suitable Green's function defined by the method of images to avoid the discretization of the infinite plane ground. This formulation, which combines the use of standard and hyper-singular integral equations over the thin bodies, is also called the dual Boundary Element Method (dual-BEM).

More recently, mesh reduction methods have been attracted great interesting of scientist for acoustics engineering problems. Among these methods, the Method of Fundamental Solutions (MFS) is a mesh-free boundary-type method and its mathematical formulation is quite simple. It is based on the prior knowledge of fundamental solutions, but not requiring the numerical and analytical integrations that need to be performed in the BEM. The MFS formulation also makes use of Green's functions and it is also very well suited to the problems of infinite and semi-infinite domains since the Sommerfeld radiation condition is automatically satisfied. However, one disadvantage of the MFS is the determination of the position of the virtual sources on which the singularities are placed. Therefore, Karageorghis [6] has proposed a simple algorithm for estimating the optimal position of the virtual sources for certain boundary value problems. Costa et al. [7, 8] have shown that, despite its simplicity, the MFS is suitable tool to efficiently predict acoustic wave propagation in the frequency domain.

This paper analyses the insertion loss of thin acoustic barriers on a rigid ground in the vicinity of a tall building by means of the MFS. The proposed formulation makes use of the sub-region technique, and the Green's functions are employed for limiting the number of discretized surfaces, consequently reducing the computational cost of the numerical model. In this model, both the ground and the building are modeled as infinite rigid plane surfaces. The proposed model is verified by the comparison of numerical results with those provided by the dual-BEM formulation. Numerical simulations are carried out by using different types of thin acoustic barriers in order to evaluate its insertion losses next to the façade of a building.

2 Governing equation

The propagation of an acoustic wave in the homogeneous linear fluid medium at rest is governed in the frequency domain by the Helmholtz equation, which can be written as:

$$\nabla^2 p(x) + k^2 p(x) = 0\,, \tag{1}$$

where $p(\mathbf{x})$ is the acoustic pressure, and $k = \omega/c$ is the wave number, with $\omega = 2\pi f$ being the angular frequency and c the speed of sound in the acoustic medium.

Assuming an infinite medium excited by a harmonic point pressure source at position $\mathbf{x}_0$, the incident pressure field at any point $\mathbf{x}$ is given by:

$$p(\mathbf{x}) = -\frac{\mathrm{i}}{4} H_0^{(2)}(kr_0), \tag{2}$$

where $r_0 = \sqrt{(x-x_0)^2 + (y-y_0)^2}$, $H_0^{(2)}$ is the Hankel function of the second kind of order zero and $\mathrm{i} = \sqrt{-1}$.

3 Image-source Green's function

In the acoustic analyses, the presence of totally reflecting plane surfaces can be taken into account by using the image-source technique. Thus, considering an image source in relation to the horizontal *x*-axis, as shown in Fig. 1(a), the corresponding Green's function can be written as:

$$G(\mathbf{x}, \mathbf{x}_0) = -\frac{\mathrm{i}}{4}\Big[H_0^{(2)}(kr_0) + H_0^{(2)}(kr_1)\Big], \tag{3}$$

with $r_1 = \sqrt{(x-x_0)^2 + (y+y_0)^2}$.

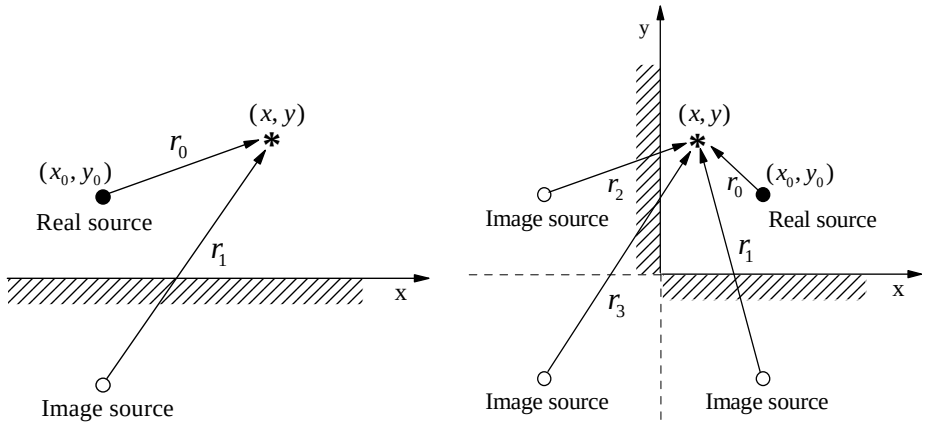

Figure 1. The image-source technique for: a) half-space; b) quarter-space and c) wedge with an opining angle β.

The above described Green's function can be further extended to incorporate more reflecting planes. Thus, considering a quarter-space defined by two axes, one at *x*-axis and other at *y*-axis, as shown in Fig. 1(b), the Green's function can be expressed as:

$$G(\mathbf{x},\mathbf{x}_0) = -\frac{\mathrm{i}}{4}\Big[H_0^{(2)}(kr_0) + H_0^{(2)}(kr_1) + H_0^{(2)}(kr_2) + H_0^{(2)}(kr_3)\Big], \tag{4}$$

with $r_2 = \sqrt{(x+x_0)^2 + (y-y_0)^2}$ and $r_3 = \sqrt{(x+x_0)^2 + (y+y_0)^2}$.

Assuming a wedge with an opining angle β, as shown in Fig. 1(c), the Green's functions can be expressed as:

$$G(\mathbf{x},\mathbf{x}_0) = -\frac{\mathrm{i}}{4}H_0^{(2)}(kr_0) - \frac{\mathrm{i}}{4}\sum_{n=1}^{NS}\Big[H_0^{(2)}(kr_1) + H_0^{(2)}(kr_2) + H_0^{(2)}(kr_3) + H_0^{(2)}(kr_4)\Big], \tag{5}$$

with $r_j = \sqrt{\big[x - r_0\cos(\gamma_j)\big]^2 + \big[y - r_0\sin(\gamma_j)\big]^2}$, $\gamma_1 = -\theta_0 - 2\beta(n-1)$, $\gamma_2 = -\theta_0 + 2\beta n$, $\gamma_3 = \theta_0 - 2\beta n$ and $\gamma_4 = \theta_0 + 2\beta n$.

where θ_0 and r_0 are the azimuth and the distance from the wedge corner to the source and *NS* is the number of sources. The number of image sources is finite because only the visible sources are taken into account. Further details on the visible sources can be found in Tadeu et al. [9] and Hasheminejad and Mojahed [10].

4 MFS Formulation

The MFS model is here developed by assuming an acoustic domain divided into *n* sub-domains, as shown in Fig. 2, in which adequate Green's functions are used. For this purpose, the collocation points placed at the circular fictitious interfaces are defined as CP and the virtual sources positioned outside each sub-region are defined as VS. Thus, within each sub-domain, the MFS allows the acoustic field to be computed as a linear combination of Green's functions, simulating the sound field within each sub-domain through a set of virtual sources located outside it and at a fixed distance from the circular interfaces that limits each sub-domain.

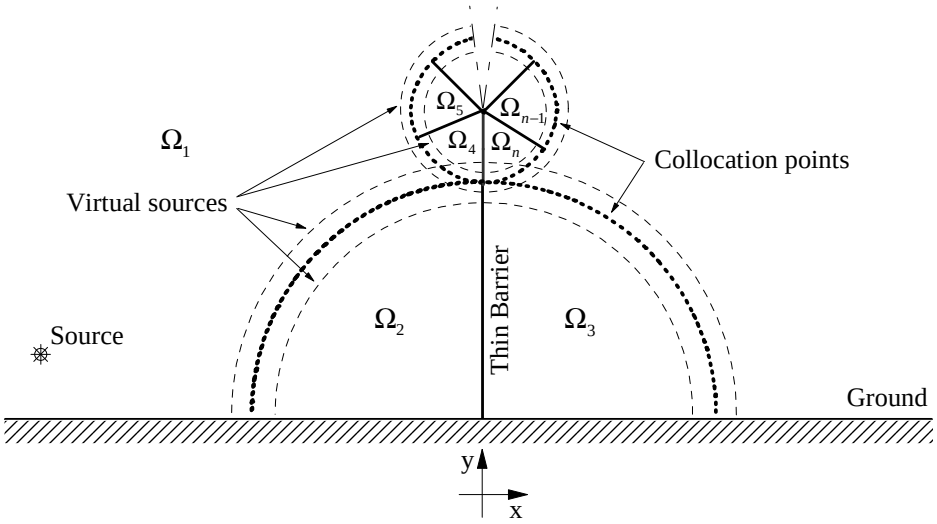

Figure 2. Schematic representation of the MFS model.

For each sub-region, the acoustic pressure at an internal point $\mathbf{x}_k$ can then be written as:

$$p(\mathbf{x}_k) = \sum_{l=1}^{VS_j} a_l^{\Omega_j} G_{kl}^{\Omega_j}(\mathbf{x}_k, \mathbf{x}_l) + \delta_{ij} G_{ks}^{\Omega_j}(\mathbf{x}_k, \mathbf{x}_s), \quad \text{within } \Omega_j (j = 1,2,3), \tag{6}$$

$$p(\mathbf{x}_k) = \sum_{l=1}^{VS_j} a_l^{\Omega_j} G_{kl}^{\Omega_j}(\mathbf{x}_k, \mathbf{x}_l), \quad \text{within } \Omega_j (j = 4,\ldots,n), \tag{7}$$

and the normal component of the particle velocity as:

$$\frac{\partial p(\mathbf{x}_k)}{\partial \mathbf{n}} = \sum_{l=1}^{\mathrm{VS}_j} a_l^{\Omega_j} \frac{\partial G_{kl}^{\Omega_j}(\mathbf{x}_k, \mathbf{x}_l)}{\partial \mathbf{n}} + \delta_{ij} \frac{\partial G_{ks}^{\Omega_j}(\mathbf{x}_k, \mathbf{x}_s)}{\partial \mathbf{n}}, \quad \text{within } \Omega_j (j = 1,2,3), \tag{8}$$

$$\frac{\partial p(\mathbf{x}_k)}{\partial \mathbf{n}} = \sum_{l=1}^{\mathrm{VS}_j} a_l^{\Omega_j} \frac{\partial G_{kl}^{\Omega_j}(\mathbf{x}_k, \mathbf{x}_l)}{\partial \mathbf{n}}, \quad \text{within } \Omega_j (j = 4,\ldots,n), \tag{9}$$

where $\mathbf{n}$ is the unit normal vector pointing outwards of each sub-region, $a_l^{\Omega_j}$ are the unknown amplitudes to be determined for each virtual source, *i* is the sub-domain in which the real source is positioned, δ_{ij} is the Kronecker delta, $G_{ks}^{\Omega_j}(\mathbf{x}_k, \mathbf{x}_s)$ is the incident field regarding the acoustic pressure generated by the real source when placed in the sub-domain Ω_j and $G_{kl}^{\Omega_j}(\mathbf{x}_k, \mathbf{x}_l)$ refers to the Green's function generated by the virtual sources. These Green's functions are obtained by means of the image-source technique, whose details were given in the previous section.

By enforcing at each collocation point $\mathbf{x}_k$, the continuity condition of the acoustic pressure and of the normal component of the particle velocity with respect to the circular fictitious interfaces, the following $2\mathrm{CP}\times 2\mathrm{VS}$ system of equations can be obtained:

$$\mathbf{A}\mathbf{x} = \mathbf{b}, \tag{10}$$

where

$$\mathbf{A} = \begin{bmatrix} \mathbf{G}^{\Omega_1}_{(k=1,\mathrm{CP}_1;l=1,\mathrm{VS}_1)} & -\mathbf{G}^{\Omega_2}_{(k=1,\mathrm{CP}_1;l=1,\mathrm{VS}_2)} & \cdots & \mathbf{0} \\ \dfrac{\partial \mathbf{G}^{\Omega_1}_{(k=1,\mathrm{CP}_1;l=1,\mathrm{VS}_1)}}{\partial \mathbf{n}} & -\mathbf{G}^{\Omega_2}_{(k=1,\mathrm{CP}_1;l=1,\mathrm{VS}_2)} & \cdots & \mathbf{0} \\ \vdots & \vdots & \ddots & \vdots \\ \mathbf{G}^{\Omega_1}_{(k=1,\mathrm{CP}_{n-1};l=1,\mathrm{VS}_1)} & \mathbf{0} & \cdots & -\mathbf{G}^{\Omega_n}_{(k=1,\mathrm{CP}_{n-1};l=1,\mathrm{VS}_n)} \\ \dfrac{\partial \mathbf{G}^{\Omega_1}_{(k=1,\mathrm{CP}_{n-1};l=1,\mathrm{VS}_1)}}{\partial \mathbf{n}} & \mathbf{0} & \cdots & -\dfrac{\partial \mathbf{G}^{\Omega_n}_{(k=1,\mathrm{CP}_{n-1};l=1,\mathrm{VS}_n)}}{\partial \mathbf{n}} \end{bmatrix}, \tag{11}$$

$$\mathbf{x} = \begin{bmatrix} \mathbf{a}^{\Omega_1}_{(l=1,\mathrm{VS}_1)} & \mathbf{a}^{\Omega_2}_{(l=1,\mathrm{VS}_2)} & \cdots & \mathbf{a}^{\Omega_n}_{(l=1,\mathrm{VS}_n)} \end{bmatrix}^T. \tag{12}$$

For example, if the real source is positioned in sub-domain Ω_1, the right-hand-side term is defined as:

$$\mathbf{b} = \begin{bmatrix} -\mathbf{G}^{\Omega_1}_{(k=1,\mathrm{CP}_1;s)} & -\dfrac{\partial}{\partial \mathbf{n}}\mathbf{G}^{\Omega_1}_{(k=1,\mathrm{CP}_1;s)} & \cdots & -\mathbf{G}^{\Omega_1}_{(k=1,\mathrm{CP}_{n-1};s)} & -\dfrac{\partial}{\partial \mathbf{n}}\mathbf{G}^{\Omega_1}_{(k=1,\mathrm{CP}_{n-1};s)} \end{bmatrix}^T, \tag{13}$$

Once this system of equations is solved, the acoustic pressure at any domain point may be obtained by using the Eqs. (6) and (7).

5 MFS validation

In order to validate the implementation of the proposed formulation, the results are compared with those provided by the standard Dual-BEM formulation. We consider thin acoustic barriers of different shapes located on a rigid ground at (0.0m, 0.0m). The fluid medium is excited by a point source placed at position (-10.0m, 1.0m), as shown in Fig. 3. The length of the upper section in each profile is 1.0m and the slope of the arms of the T- and Y-profiles is 45^o. The effective height of the T- and Y-profile barriers is 2.0m. In this analysis, a plain thin barrier 2.0m height is also considered. The acoustic medium is assumed to be air at 20 ^oC and atmospheric pressure of 1atm, with density of $1.21 kgm^{-3}$ and sound propagation velocity of $343 ms^{-1}$. Here, computations are performed for frequencies up to 1000Hz, with a frequency step of 25Hz. A dual-BEM model is used as a reference model for comparison of the computed results of the proposed model. This model was discretized with a very large number of elements (about 50 elements per wavelength) to ensure the accuracy of the numerical solution. The number of collocation points is defined by means of the relation between the incident wavelength and distance between collocation points. This relation is defined as *r*. The distance between the virtual sources and the fictitious circular interface is defined as D_{vs} and the distance of the collocation points is defined as D_{cp}. In all results, the number of virtual sources is equal to the number of collocation points, and a distance between collocation and source points of $D_{vs}=2.0D_{cp}$ is always used. Further details on this distance can be found in Costa et al. [11].

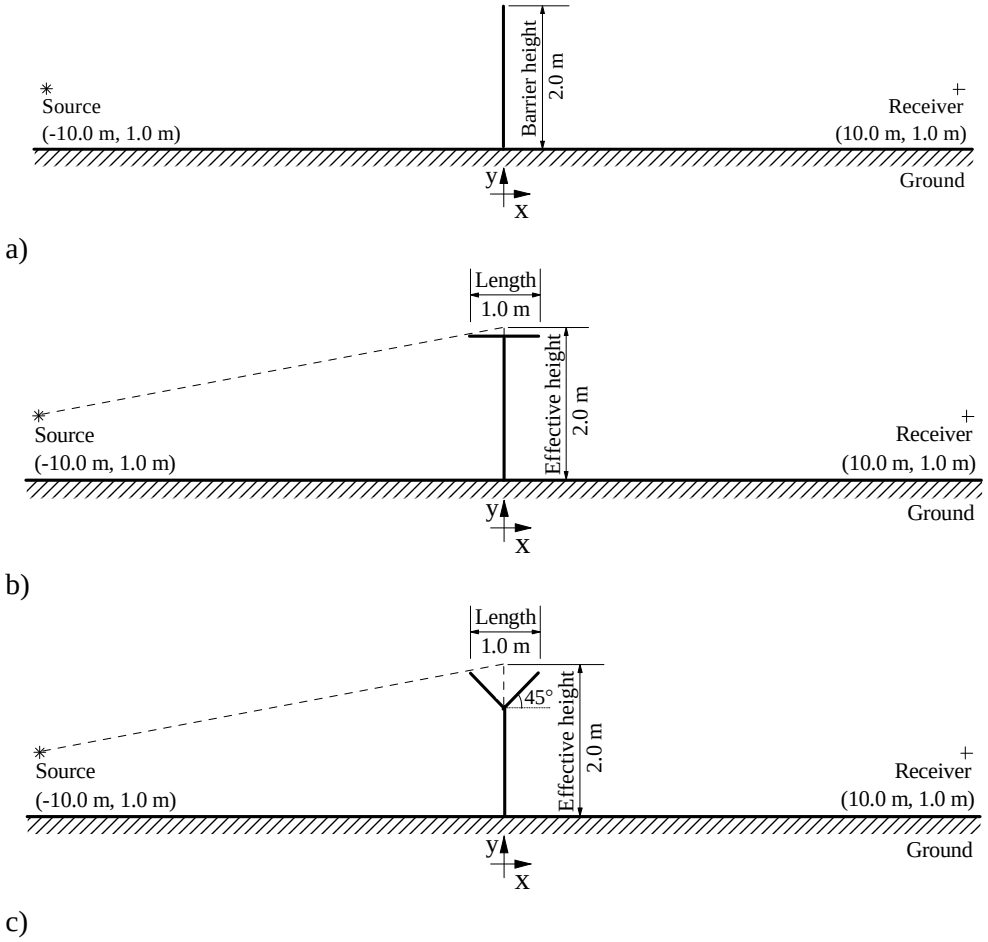

Figure 3. Geometry of the problem considering different types of thin acoustic barriers: a) Plain, b) T and c) Y.

Figure 4 displays the comparison between the dual-BEM and the MFS results as a function of the frequency range 50-1000Hz, with a frequency step of 25Hz. A logarithmic scale was used to allow a better observation of the difference between acoustic pressure amplitudes of the MFS and the reference solutions. Analysis of the results clearly confirms that as the relation *r* increases, an

excellent agreement among the two solutions is obtained (see Fig. 4(a1-c1)). The results presented in Fig. 4(a2-c2) show that the MFS response converges to the reference solution as the relation *r* increases. This behavior indicates the good accuracy of the MFS model with respect to the relation *r* for a fixed distance between the virtual sources and the fictitious circular interfaces.

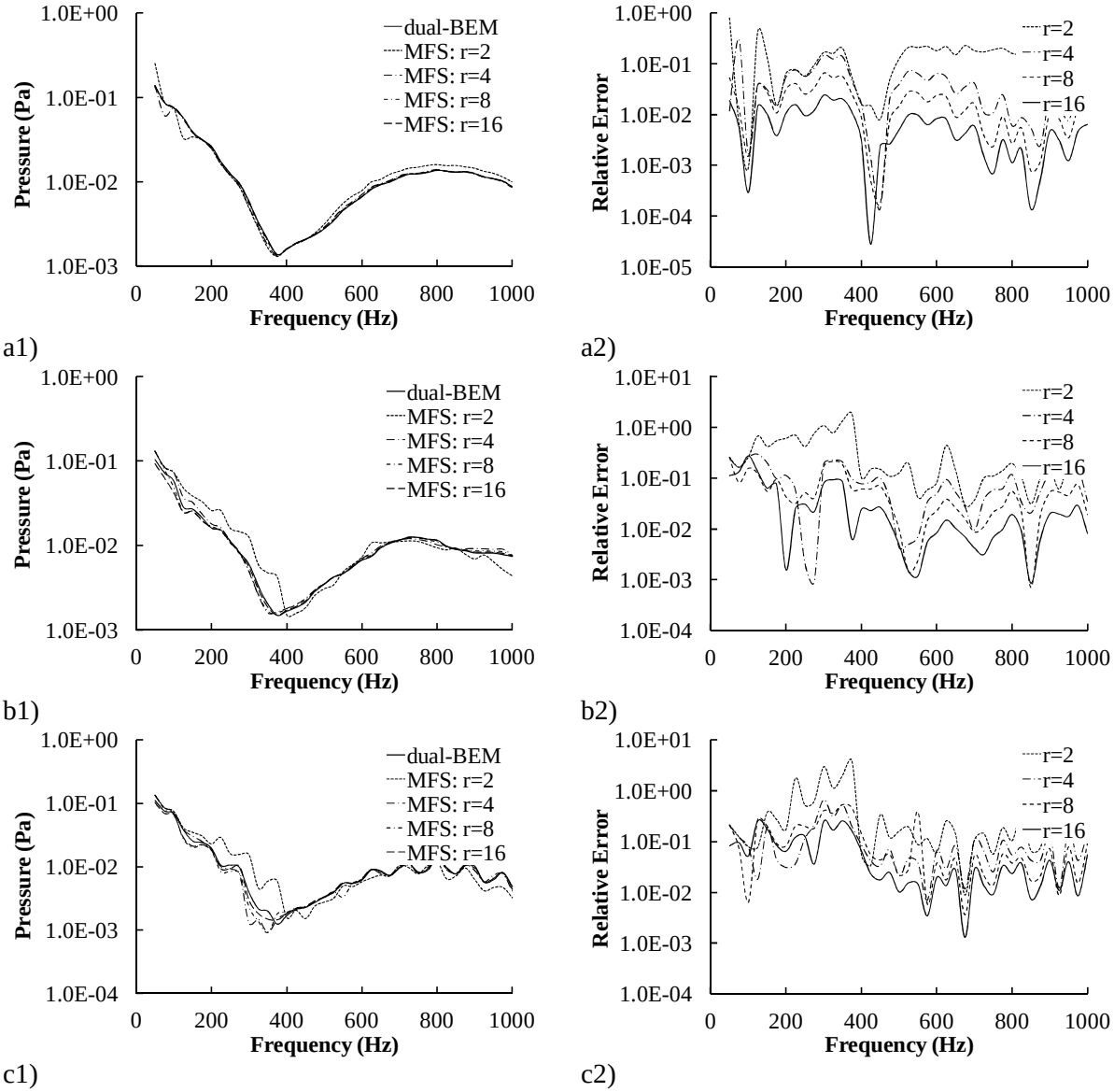

Figure 4. Dual-BEM and MFS results as a function of the frequency range 50-1000Hz for different relations between incident wavelength and spacing between collocation points, considering different types of thin acoustic barriers: a) Plain, b) T and c) Y.

6 Numerical examples

In order to show the applicability of the proposed formulation, the problem is analysed in this section using thin acoustic barriers of different shapes on a rigid ground. Once again, the length of the upper section for each profile is 1.0m and the slope of the arms of the T- and Y-profiles is 45^{o}. The effective height of the T- and Y-profile barriers is 2.0m. In this example, the response provided by a plain thin barrier 2.0m height is displayed and used as a reference solution. The simulations are analysed for the1/3rd octave frequency bands of 500Hz and 1000Hz, which are commonly used for traffic noise. Here, an excitation source is placed at position (-3.0m, 0.5m) and the barriers are located at position (0.0m, 0.0m), as shown in Fig. 5. Again, the acoustic medium is assumed to be air at 20 ^{o}C and atmospheric pressure of 1atm, with density of 1.21kgm^{-3} and sound propagation velocity of

343ms^{-1}. The Insertion Loss ($\mathrm{IL} = -20\mathrm{Log}_{10}\left(\left|p\right|/\left|p_0\right|\right)$ with p_0 being the acoustic pressure generated by a point source without the presence of the barrier) is used to show the influence of the thin noise barrier on an infinite rigid ground. In this example, IL values are calculated at a set of receivers located along a vertical line 0.5m away from the building. The virtual sources are placed at $D_{vs}=2.0D_{cp}$ from the circular fictitious interfaces, and a relation of 50 was always used to ensure the accuracy of the numerical method. In this example, both the ground and the building are treated as infinite plane surfaces, and the thin acoustic barrier is placed 30.0m from the façade of a building.

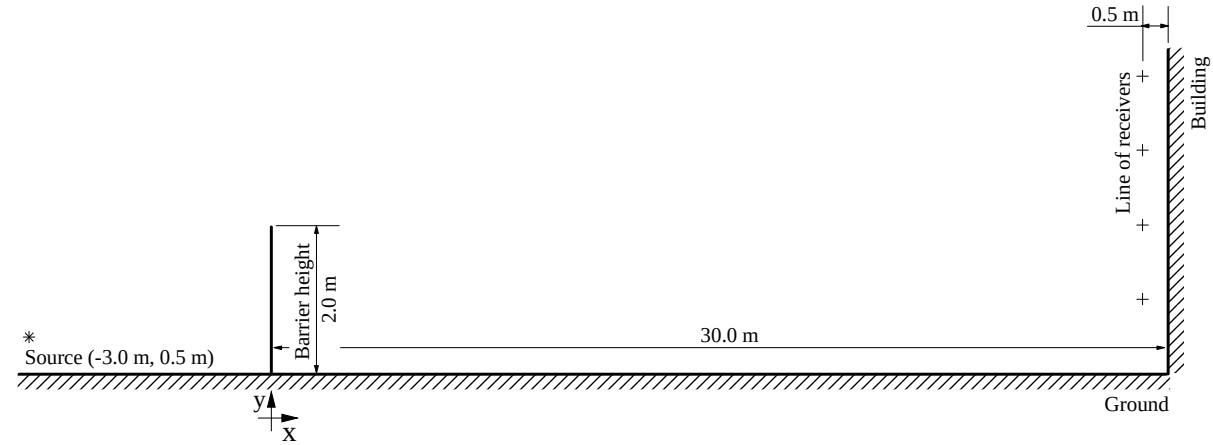

a)

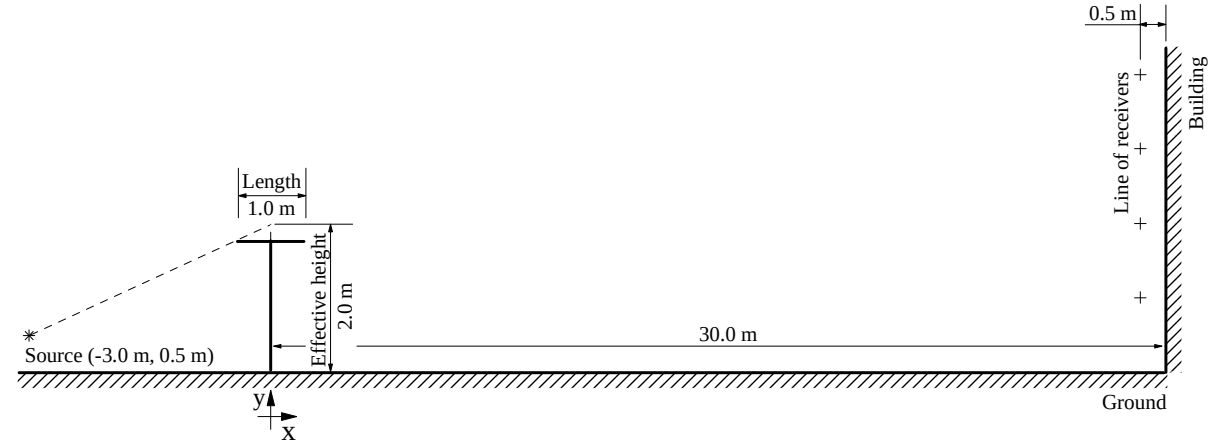

b)

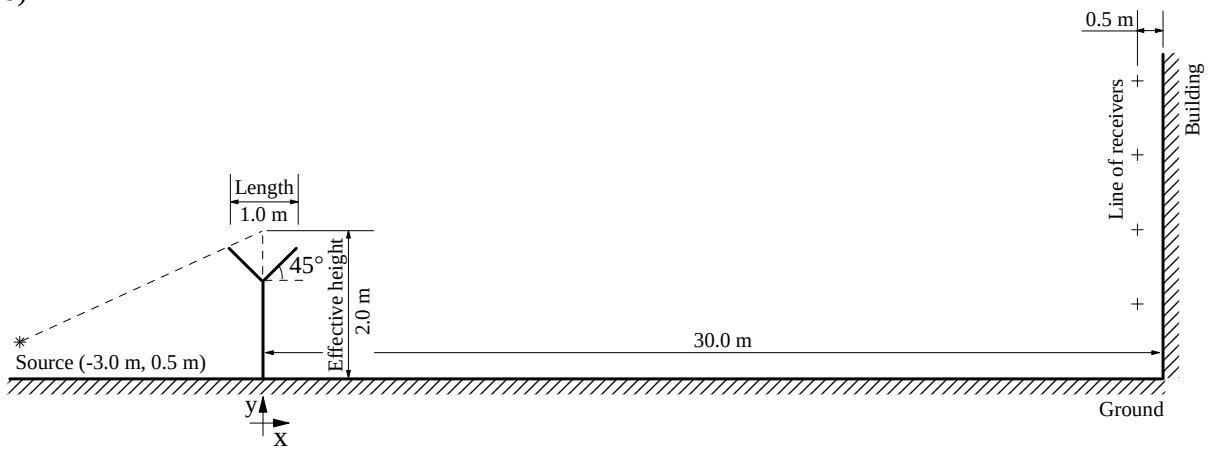

c)

Figure 5. Geometry of the problem considering different types of thin acoustic barriers: a) Plain, b) T, and c) Y.

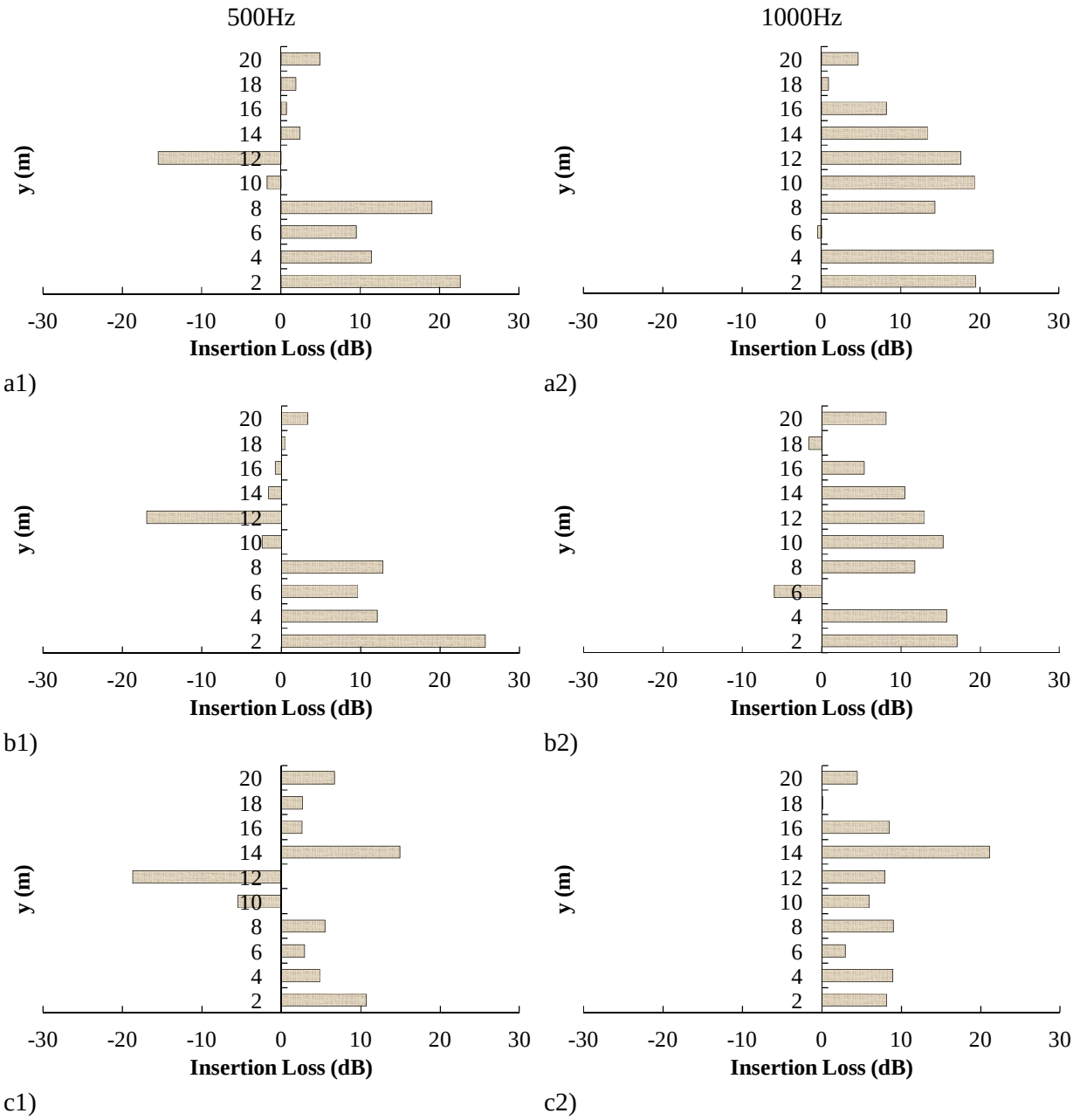

Figure 6. IL values at a set of receivers located along a vertical line 0.5 m away from the building for the 1/3rd octave frequency bands of 500Hz and 1000Hz, considering different types of thin acoustic barriers: a) Plain, b) T and c) Y.

Figure 6 exhibits the IL values for thin acoustic barriers of different profiles on a rigid ground for the 1/3rd octave frequency bands of 500Hz and 1000Hz. Analysis of these results reveals increased IL values for the receivers placed close to the ground, except for the Y-shaped barriers that present reduced IL values as the distance to the ground decreases. After reaching the maximum performance, all the barriers become less efficient and thus a negative contribution may also be observed. This negative contribution is more pronounced at y=12.0m for the frequency band of 500Hz (see Figs. 6(a1-c1)). It is interesting to note that the T-profiles present a very similar behavior with respect to the plain barriers, with reductions of near 5dB being registered, in specific points. However, the T-profile provides a maximum IL value of 25.7dB at y=2.0m for the frequency band of 500Hz (see Fig. (b1)). Analysing the Y-profiles, some differences can be identified with respect to the plain and T-profile barriers. In this case, the Y-profile barriers are less well efficient for the receivers placed below 10.0m, except at y=6.0m for the frequency band of 1000Hz (see Fig. (c2)). However, for the frequency band of 500Hz, the acoustic performance of these barriers improves as the distance to the ground increases

(see Fig. 6(c1)), and for the frequency band of 1000Hz, this improvement only occurs at y=14.0m (see Fig. 6(c2)). It is important to note that, in general, the thin acoustic barriers are more efficient for the frequency band of 1000Hz, thus leading to a greater attenuation of the sound pressure level near the façade.

7 Conclusions

In this paper, a two-dimensional numerical model based on the Method of Fundamental Solutions was presented and used to predict the insertion loss of thin acoustic barriers on a rigid plane ground in the vicinity of a tall building. The proposed formulation made use of adequate Greens functions defined by the image-source technique, which allowed a significant reduction of the computational cost of the numerical model. The MFS was implemented and verified against the classical Dual-BEM formulation, revealing good accuracy of the proposed formulation. Numerical simulations were performed by using different types of thin barriers, evaluating its insertion losses next to the building façade.

This analysis makes it clear that the MFS is a very interesting tool to efficiently predict the acoustic performance of thin barriers of different shapes.

Acknowledgements

The authors acknowledge the financial support of Conselho Nacional de Desenvolvimento Científico e Tecnológico (CNPq). This study was also financed in part by the Coordenação de Aperfeiçoamento de Pessoal de Nível Superior – Brasil (CAPES) – Finance Code 001.

References

[1] C.A. Brebbia. *The Boundary Element Method For Engineers*, London: Pentech Press, 1984.
[2] P. Filippi. G. Dumery, Etude Théorique et Numérique de la Diffraction par un Écran Mince. *Acustica*, vol. 21, pp. 343-359, 1969.
[3] F. Cassot. Contribuition à L'étude de la Diffraction par un Écran Mince, *Acoustica*, vol. 34, pp. 64-71, 1975.
[4] T. Terai. On Calculation of Sound Fields around Three-dimensional Objects by Integral Equation Methods, *Journal of Sound and Vibration*, vol. 69, pp. 71-100, 1980.
[5] Y. Kawai, T. Terai. The Application of Integral Equation Methods to the Calculation of Sound Attenuation by Barriers, *Applied Acoustics*, vol. 31, pp. 101-117, 1990.
[6] A. Karageorghis. A Practical Algorithm for Determining the Optimal Pseudo-Boundary in the Method of Fundamental Solutions, *Advances in Applied Mathematics and Mechanics*, vol. 1, no. 4, pp. 510-528, 2009.
[7] E.G.A. Costa, J.A.F. Santiago, L.M.C. Godinho, L.C. Wrobel, W.J. Mansur. Three Efficient Numerical Models to Analyse the Step Problem in Shallow Water, *Engineering Analysis with Boundary Elements*, vol. 62, pp. 44-56, 2016.
[8] E.G.A. Costa, L. Godinho, J. A. F. Santiago, W.J. Mansur. Efficient Model for Acoustic Attenuators using the Method of Fundamental Solutions, *International Journal of Acoustics and Vibration*, vol. 23, no. 1, pp. 74-82, 2018.
[9] A. Tadeu, E.G.A. Costa, J. António, P. Amado-Mendes. 2.5D and 3D Green's Functions For Acoustic Wedges: Image Source Technique Versus A Normal Mode Approach, *Journal of Computational Acoustics*, vol. 21, no. 1, pp. 1250025, 2013.
[10] S.M. Hasheminejad and A. Mojahed. Transient sound radiation from an impulsively excited piezoelectric composite hollow sphere in a wedge-shaped acoustic domain, *Wave Motion*, vol. 62, pp. 1-19, 2016.

[11] E.G.A. Costa, L.M.C. Godinho, J.A.F. Santiago, W.J. Mansur, F.C. Peters. Application of the Method of Fundamental Solutions to Predict the Acoustic Performance of T-Shaped Thin Barriers *Engineering Analysis with Boundary Elements*, vol. 99, pp. 142-156, 2019.